Nanoscale Phase Separation and High Photovoltaic Efficiency in Solution-Processed, Small-Molecule Bulk Heterojunction Solar Cells

By *Bright Walker, Arnold B. Tamayo, Xuan-Dung Dang, Peter Zalar, Jung Hwa Seo, Andres Garcia, Mananya Tantiwiwat,* and *Thuc-Quyen Nguyen**

Research relating to organic solar cells based on solution-processed, bulk heterojunction (BHJ) films has been dominated by polymeric donor materials, as they typically have better film-forming characteristics and film morphology than their small-molecule counterparts. Despite these morphological advantages, semiconducting polymers suffer from synthetic reproducibility and difficult purification procedures, which hinder their commercial viability. Here, a non-polymeric, diketopyrrolopyrrole-based donor material that can be solution processed with a fullerene acceptor to produce good quality films is reported. Thermal annealing leads to suitable phase separation and material distribution so that highly effective BHJ morphologies are obtained. The frontier orbitals of the material are well aligned with those of the fullerene acceptor, allowing efficient electron transfer and suitable open-circuit voltages, leading to power conversion efficiencies of 4.4 ± 0.4% under AM1.5G illumination (100 mW cm^{-2}). Small molecules can therefore be solution processed to form high-quality BHJ films, which may be used for low-cost, flexible organic solar cells.

1. Introduction

Bulk heterojunction (BHJ) solar cells comprising interpenetrating networks of an organic donor and a fullerene derivative acceptor such as [6,6]-phenyl-C_{61}-butyric acid methyl ester ($PC_{61}BM$) constitute a promising technology because they are easy to fabricate by solution processing and are predicted to yield power conversion efficiencies (PCEs) of up to 10% if a suitable low band-gap donor material is discovered.[1] Although considerable research effort has been expended to develop such low band-gap donor materials,[2] the highest reported efficiencies have been dominated by conjugated polymers such as poly(3-hexylthiophene) (P3HT).[3–6] This system has been explored thoroughly for the past decade and yields PCEs up to 5%. The high efficiency of P3HT–fullerene devices can be explained by the ability of the blend to phase separate and crystallize into desirable BHJ morphologies after processing, allowing for efficient charge separation and transport.[7,8]

The majority of research relating to BHJ solar cells has focused on polymeric donor materials, since they generally have better film-forming properties than non-polymeric materials.[9] Small-molecule donor materials can also form useable BHJ solar cells by solution processing, although it is more challenging to obtain high-quality films. The highest reported efficiencies for such devices have remained low (PCEs range from 0.3% to 1.7%) relative to solution processed solar cells using polymeric donor materials (~5%). Small-molecule materials, however, offer advantages over polymeric materials in terms of ease of synthesis and purification, which greatly improve fabrication reproducibility, as well as possessing a greater tendency to self-assemble into ordered domains, which leads to high charge carrier mobilities.[10,11] Small molecules do not suffer from batch to batch variations, broad molecular-weight distributions, end-group contamination, or difficult purification methods, which can be significant problems for polymeric materials. These considerations make small molecules a promising class of donor material for BHJ solar cell applications.[12–20]

Recently, our group reported a new class of small molecules based on diketopyrrolopyrrole (DPP) and oligothiophene (OT) building blocks. The DPP moiety imparts high optical density while its electron affinity lowers frontier energy levels to complement those of [6,6]-phenyl-C_{71}-butyric acid methyl ester (**$PC_{71}BM$**). Concurrently, the OT portion imparts electron donating character and high hole mobility.[21–23] The DPP–thiophene motif also provides locations for structural modification so to tailor electronic and optical properties. For example, by adjusting the number of thiophenes, the film absorption can shift up to 100 nm. Introducing solubilizing group onto the aryl groups bound to the DPP core leads to films that self-assemble into ordered domains,[24] which can be fabricated into field-effect transistors

[*] Prof. T.-Q. Nguyen, B. Walker, Dr. A. B. Tamayo, Dr. X.-D. Dang, P. Zalar, Dr. J. H. Seo, A. Garcia
Center for Polymers and Organic Solids
Department of Chemistry and Biochemistry
University of California
Santa Barbara, CA 93106 (USA)
E-mail: quyen@chem.ucsb.edu
M. Tantiwiwat
Department of Physics
University of California
Santa Barbara, CA, 93106 (USA)

DOI: 10.1002/adfm.200900832

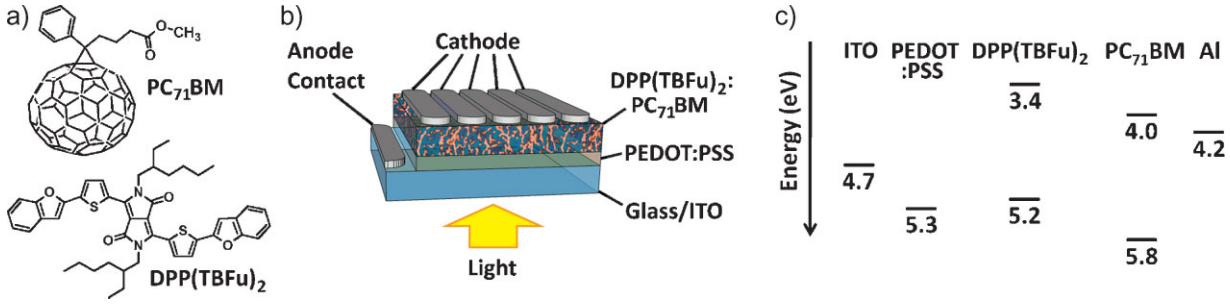

Figure 1. Schematic diagrams. a) Chemical structures, b) device architecture, and c) energy levels.

with high mobilities[25] and that can be used to fabricate efficient BHJ solar cells.[26] Until now, the highest published PCE for solution-processed small-molecule-based solar cells (3.0%) has been achieved by our group using a 2-ethylhexyl-substituted DPP core functionalized with two thiophene trimers.[27]

To improve the PCE value of BHJ solar cells using DPP–OT materials, we targeted increasing the open-circuit voltage (V_{OC}). Previous studies on conjugated polymer BHJ cells have shown that the difference between the highest occupied molecular orbitals (HOMO) of the donor and lowest unoccupied molecular orbitals (LUMO) of the acceptor largely determines the V_{OC}.[28–30,1] The LUMO level of the acceptor should be at least 0.3 eV lower than that of the donor to drive charge separation after exciton formation. An offset greater than 0.3 eV results in wasted energy during electron transfer.[7,31,32] Based on these considerations we envisioned using a fused benzofuran system to replace the terminal bithiophene units from our previous structural design. The fused system maintains a highly conjugated structure while the electronegative oxygen atom stabilizes the HOMO of the molecule. We found that solution processed films of the benzofuran-substituted DPP–OT–3,6-bis(5-(benzofuran-2-yl)thiophen-2-yl)-2,5-bis(2-ethylhexyl)pyrrolo[3,4-c]pyrrole-1,4-dione (**DPP(TBFu)$_2$**) have good absorption properties and frontier energy levels that are appropriately aligned with those of **PC$_{71}$BM**—a commonly used acceptor molecule in BHJ solar cells (Fig. 1). **DPP(TBFu)$_2$:PC$_{71}$BM** mixtures form good quality films and can self assemble into BHJ morphologies with bi-continuous networks of donor and acceptor rich domains after annealing. Annealed **DPP(TBFu)$_2$:PC$_{71}$BM** devices yield PCEs of up to 4.4 ± 0.4 % with V_{OC} of 0.9V. We justify the performance of the material based on its frontier orbital energies, light absorption, and film-forming characteristics.

2. Results and Discussion

2.1. Optical and Electronic Properties

Figure 2 shows the absorption of pure **DPP(TBFu)$_2$** solution and films, a pure **PC$_{71}$BM** film and **DPP(TBFu)$_2$:PC$_{71}$BM** films as a function of annealing temperatures and blend ratios. **DPP(TBFu)$_2$** absorbs past 650 nm in solution with a molar absorptivity of 64 000 $M^{-1}cm^{-1}$ at 630 nm. The absorption broadens and extends to 710 nm in the solid state (Fig. 2a). The absorption spectrum of pure **DPP(TBFu)$_2$** changes considerably after thermal annealing, as shown in Figure 2b. A significant increase in absorption intensity at 590 nm occurs after thermal annealing up to 100 °C, followed by a decrease in intensity above 100 °C. Increases in optical absorption after annealing have been observed for P3HT and are found to derive from aggregation/interchain interactions and an increase in the crystallinity of the material, which enhances the probability of optically active π–π* electronic transitions.[33–35]

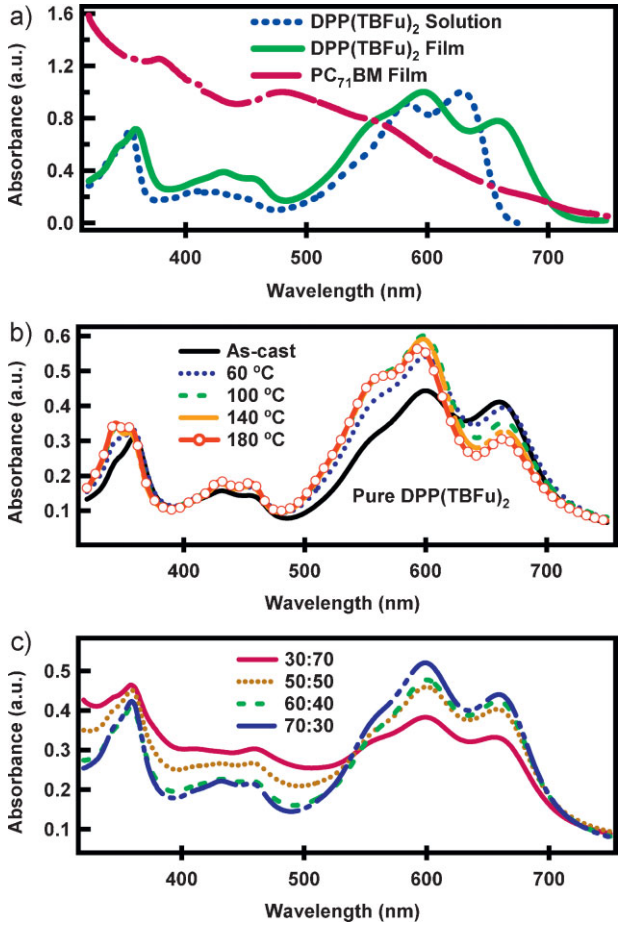

Figure 2. UV–Vis absorption spectra. a) Pure **DPP(TBFu)$_2$** in solution and solid state and pure **PC$_{71}$BM** film. b) Pure **DPP(TBFu)$_2$** films after annealing at different temperatures. c) As-cast films composed of different donor–acceptor ratios.

An increase in the crystallinity of annealed **DPP(TBFu)$_2$** was also confirmed by X-ray diffraction (XRD) studies (Supporting Information, Fig. S1). XRD data show an increase in the diffraction intensity, which implies a higher degree of crystallinity after heating at 100 °C. The absorption of the blend at various annealing temperature shows a similar trend in the 500–700 nm region as that observed in the pure film.

Absorption characteristics of as-cast **DPP(TBFu)$_2$:PC$_{71}$BM** films at various blend ratios are shown in Figure 2c. It can be seen that mixtures of the two materials absorb strongly throughout the range of 300 nm to 700 nm. The absorption of the blends is relatively high in the 500 to 700 nm range for all blend ratios, reflecting the higher optical density of **DPP(TBFu)$_2$** relative to **PC$_{71}$BM**. The **DPP(TBFu)$_2$** absorption (500 to 700 nm) increases with increasing donor content, while the **PC$_{71}$BM** absorption decreases with lower acceptor content in the blends.

The HOMO level of **DPP(TBFu)$_2$** was determined to be 5.2 eV by using ultraviolet photoelectron spectroscopy (UPS)[36,37] and was not found to change significantly when mixed with **PC$_{71}$BM** (Supporting Information, Fig. S2). The band gap estimated from the onset of the absorption spectrum (710 nm) was found to be 1.7 eV (Fig. 2a), putting the LUMO of the material at approximately 3.4 eV. The HOMO, band gap and LUMO of **PC$_{71}$BM** film were measured using the same techniques, and found to be 5.8, 1.8, and 4.0 eV, respectively (Fig. 1b), similar to previously reported values for fullerenes.[38] The difference between the LUMO of **PC$_{71}$BM** and HOMO of **DPP(TBFu)$_2$** is 1.2 eV, and is expected to yield a V_{OC} on the order of 0.9 V.[1,39]

2.2 Film Morphologies

We investigated the morphologies of pure **DPP(TBFu)$_2$** films and blends with **PC$_{71}$BM** by using tapping-mode atomic-force microscopy (AFM). **DPP(TBFu)$_2$** is soluble in chloroform and forms smooth films with an average surface roughness of 0.7 nm when spin-coated atop indium tin oxide (ITO)-coated glass substrates with a 45-nm layer of poly(styrenesulfonic acid)-doped poly(ethylenedioxythiophene) (PEDOT:PSS). Annealing pure **DPP(TBFu)$_2$** at 100 °C increases surface roughness to ~1.0 nm (Supporting Information, Fig. S3a and b).

Next, we examine the surface structure of **DPP(TBFu)$_2$:PC$_{71}$BM** films as a function of annealing temperature by using AFM. Figure 3 shows the topographic and phase images of as-cast and annealed 70:30 **DPP(TBFu)$_2$:PC$_{71}$BM** films. The topographic and phase images of the as-cast films are featureless with a surface roughness of ~0.5 nm (Fig. 3a and d). Thermal annealing at temperatures above 80 °C results in significant changes in the surface morphology. Figure 3 depicts the topography of a 70:30 **DPP(TBFu)$_2$:PC$_{71}$BM** blend ratio after heating at 90 °C and 100 °C for 10 min in nitrogen. The topographic image of **DPP(TBFu)$_2$:PC$_{71}$BM** annealed at 90 °C comprises small oblong domains 10–50 nm wide with a surface roughness of ~1.1 nm (Fig. 3b). These oblong domains increase in average size to ~100 nm upon thermal annealing at 100 °C, and the surface roughness is ~2.3 nm (Fig. 3c). Similar changes in the film morphology upon thermal annealing are observed for other blend ratios as well.

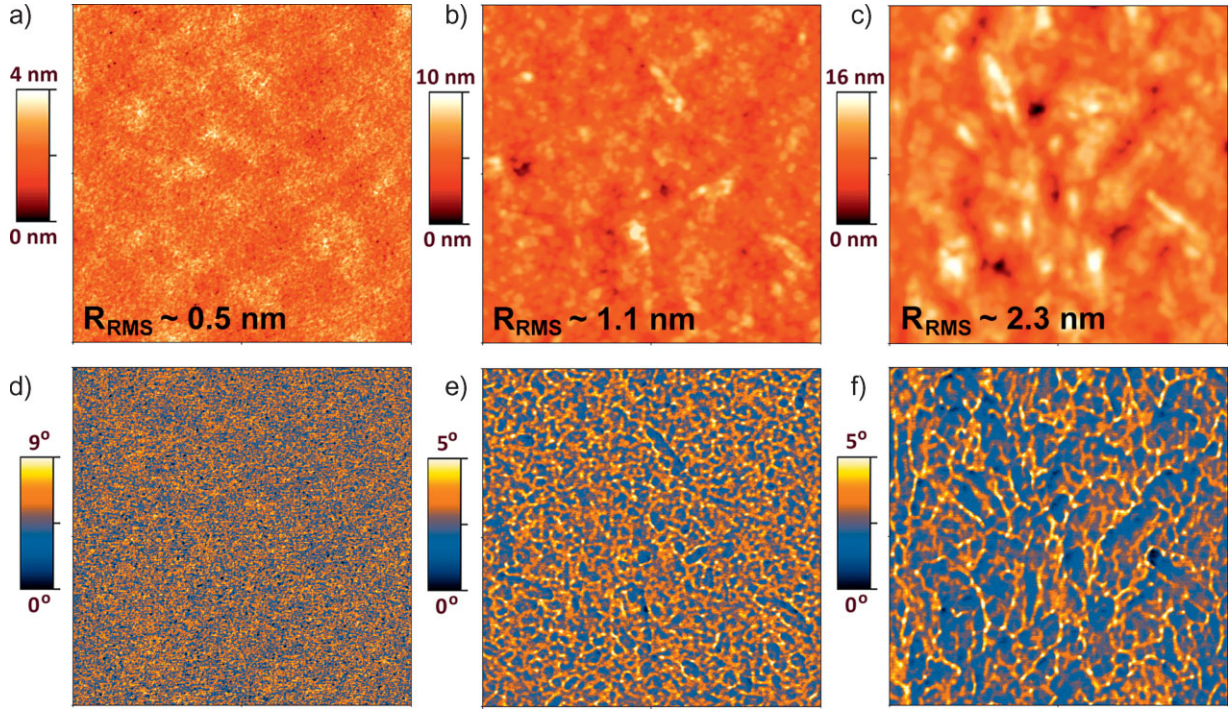

Figure 3. AFM images of 70:30 **DPP(TBFu)$_2$:PC$_{71}$BM** films spin-coated on ITO/PEDOT:PSS substrates and annealed at various temperatures. a–c) Height images of as-cast film (a), film after annealing at 90 °C (b), and at 100 °C (c). d–f) Phase images of films as-cast (d), annealed at 90 °C (e), and at 100 °C (f). It can be seen that the size of the surface features increases with annealing temperature. The scan size for all images is 2 μm × 2 μm.

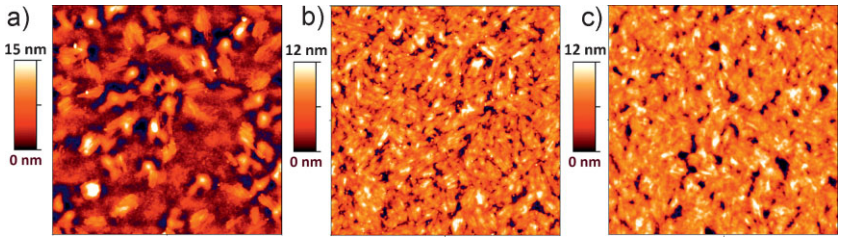

Figure 4. AFM images of **DPP(TBFu)$_2$:PC$_{71}$BM** films spin-coated on ITO/PEDOT:PSS substrates and annealed at 100 °C for 10 minutes. a–c) Height images for 30:70 (a), 50:50 (b), and 70:30 (c) blend ratios. The scan size for all images is 5 μm × 5 μm.

Figure 3e and f shows the corresponding phase images of the annealed 70:30 **DPP(TBFu)$_2$:PC$_{71}$BM** blend. Two distinct domains (orange and blue in figure) are observed to form. We assign the blue phase to a donor-rich material and the orange phase to an acceptor-rich material because the blue-phase and the orange-phase domains increase with the donor and the acceptor content, respectively. There is a clear dependence between the annealing temperature and the domain size, where the average domain size of the donor material increases from several ten of nanometers when annealing at 90 °C (Fig. 3e) to hundreds of nanometers at 100 °C (Fig. 3f). Thus, the surface domain sizes of a given blend can be controlled by varying the annealing temperature.[40] The observed changes in morphology agree well with the absorption and XRD results.

Next, we examine the effect of donor:acceptor ratio on film morphology of the as-cast and annealed blends: 30:70, 50:50, 60:40, and 70:30. The as-cast **DPP(TBFu)$_2$:PC$_{71}$BM** films at various blend ratios are smooth with a surface roughness of less than 1 nm and are similar to those shown in Figure 3a and d (see Supporting Information Fig. S3c and d). Figure 4 shows the topographic images at various blend ratios after heating at 100 °C for 10 min. The 30:70 blend exhibits isolated clusters of rod-like domains of **DPP(TBFu)$_2$** within the **PC$_{71}$BM** matrix (Fig. 4a). The average width and length of the rod-like structures are ~80 nm and 440 nm, respectively, while the average surface roughness is 2.3 nm. At a 50:50 ratio, the entire surface is covered with rectangular clusters of rod-like domains (Fig. 4b), with a surface roughness of 2.1 nm. The dimensions of the rod-shaped features are similar to those observed in the 30:70 ratio. The 70:30 ratio shows a morphology that is similar, albeit less defined, to that observed in the 50:50 ratio (Fig. 4c).

2.3. Charge Carrier Mobilities

Low charge carrier mobilities result in charge accumulation and inefficient charge collection while unbalanced charge carrier mobilities decrease the fill factor (*FF*) and efficiency of BHJ devices by promoting charge recombination.[41,42] To quantify carrier mobilities for the **DPP(TBFu)$_2$:PC$_{71}$BM** films, current-density–voltage (*J–V*) characteristics of single-carrier diodes were measured for pure and blended materials. The hole and electron mobilities were extracted using the space-charge limited current (SCLC) model.[43–45] Pure **DPP(TBFu)$_2$** films exhibit hole mobilities on the order of ~1×10^{-5} cm^2 V^{-1} s^{-1} before and after annealing at 100 °C (Supporting Information, Fig. S4a). For the blends, the average hole mobilities for as-cast 30:70, 50:50, 60:40, and 70:30 films were found to be 0.9×10^{-5} cm^2 V^{-1} s^{-1}, 2×10^{-5} cm^2 V^{-1} s^{-1}, 3×10^{-5} cm^2 V^{-1} s^{-1}, and 3×10^{-5} cm^2 V^{-1} s^{-1}, respectively. The hole mobilities did not change significantly upon annealing. Electron mobilities were found to increase significantly with higher acceptor concentration from 2×10^{-5} cm^2 V^{-1} s^{-1} to 70×10^{-5} cm^2 V^{-1} s^{-1} to 200×10^{-5} cm^2 V^{-1} s^{-1} for the 70:30, 50:50 and 30:70 blend ratios, respectively. After annealing at 100 °C, the electron mobility increases by a factor of 45 for the 70:30 blend (90×10^{-5} cm^2 V^{-1} s^{-1}) but there is only a slight improvement in electron mobilities for the 50:50 and 70:30 blend ratios (200×10^{-5} cm^2 V^{-1} s^{-1} and 300×10^{-5} cm^2 V^{-1} s^{-1}, respectively). One possible explanation for these observations is that percolation pathways are poorly formed at low fullerene concentrations, but improve upon thermal annealing. When a sufficiently high fraction of the fullerene component, that is, 30:70, is used, the percolation pathways are obtained directly from solution. The plot of the charge carrier mobility versus the blend ratio before and after annealing is included in the Supporting Information (Fig. S4b). The carrier mobility was found to be more balanced at high donor concentrations (60:40 and 70:30 blend ratios), and is perhaps one of the factors that contributes to higher device performance, as described in more detail below.

2.4. Device Properties

After understanding thin-film properties, we examine how the **DPP(TBFu)$_2$:PC$_{71}$BM** films perform in solar cells. Figure 5 shows the *J–V* and the incident-photon conversion efficiency (IPCE) characteristics of as-cast and annealed **DPP(TBFu)$_2$:PC$_{71}$BM** (60:40) devices under AM 1.5G illumination at an intensity of 100 mW cm^{-2}. The short-circuit current density (J_{SC}), V_{OC}, and *FF* for all devices are summarized in Table 1. The V_{OC} is ~0.9 V and remains unchanged for all annealing temperatures and donor:-acceptor blend ratios. The J_{SC} is small for as-cast 60:40 blended films (1.5 mA cm^{-2}) and increases substantially to a value of 8.9 mA cm^{-2} for devices annealed at 80 °C (Table 1). The J_{SC} reaches a maximum value of 10 mA cm^{-2} after annealing at 110 °C, a factor of 6 higher than for the as-cast devices. The J_{SC} decreases slightly to 8.3 mA cm^{-2} after annealing at 150 °C (Table 1). The slight drop in J_{SC} is likely a result of decreased charge separation due to a reduced donor–acceptor interfacial area, consistent with the observed change in the donor and the acceptor domain sizes from the AFM images collected at high annealing temperatures, Figure 3c. The *FF* shows the same trend as the J_{SC}. The *FF* is 0.24 for as-cast devices and increases to 0.38 for devices annealed at 80 °C (Table 1). The *FF* reaches a maximum value of 0.48 for devices annealed at 110 °C and decreases slightly to 0.46 for those annealed at 150 °C. The improved J_{SC} and *FF* of the device annealed at 110 °C leads to an efficiency of 4.4%, over an order of magnitude higher than the as-cast device (0.33%; Table 1).

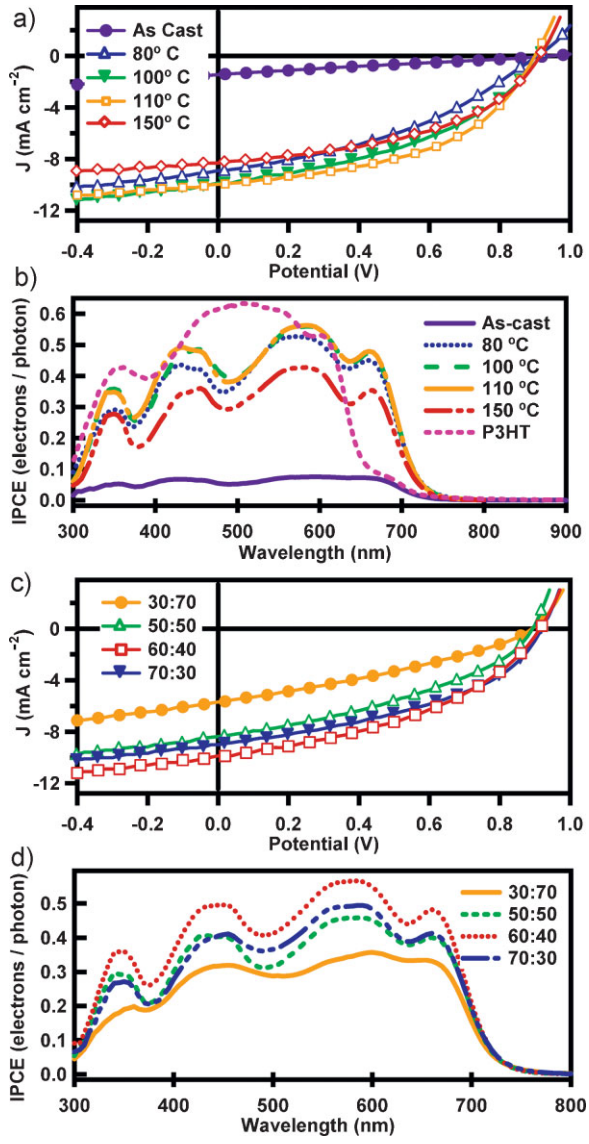

Figure 5. *J–V* characteristics and external quantum efficiencies of **DPP(TBFu)$_2$:PC$_{71}$BM** devices. a) *J–V* curves of a 60:40 **DPP(TBFu)$_2$:PC$_{71}$BM** blend ratio annealed at different temperatures. b) IPCE spectra of a 60:40 **DPP(TBFu)$_2$:PC$_{71}$BM** blend annealed at different temperatures compared to a **P3HT:PC$_{61}$BM** device. c) *J–V* curves of different **DPP(TBFu)$_2$:PC$_{71}$BM** blend ratios after annealing at 100 °C. d) IPCE spectra of different **DPP(TBFu)$_2$:PC$_{71}$BM** blend ratios after annealing at 100 °C.

The IPCEs of a 60:40 blend ratio at various annealing temperatures are shown in Figure 5b. Integrating the IPCE yields the theoretical J_{SC} values, which equal the measured values in the *J–V* curves to ± 1 mA cm^{-2}. The IPCE of a 1:1 P3HT:PC$_{61}$BM device is included for comparison (dashed line). The IPCEs of the **DPP(TBFu)$_2$:PC$_{71}$BM** devices extend past 700 nm. The IPCE of the as-cast **DPP(TBFu)$_2$:PC$_{71}$BM** device is around 10%. The IPCE of the 60:40 device annealed at 100 °C integrates to 10 mA cm^{-2}, similar to the measured J_{SC} (Fig. 5a) and reaches a maximum of 58% at 585 nm. The shape of the IPCE spectrum resembles the shape of the absorption spectrum of the blended films, with the notable exception that the relative height of the IPCE plot in the 350–500 nm region is higher than the absorption. Perhaps the excitons generated by **PC$_{71}$BM** are harvested more efficiently than the donor due to the smaller **PC$_{71}$BM** domain sizes as seen in the AFM images (Fig. 3).

Table 1. Comparison of device characteristics of different **DPP(TBFu)$_2$:PC$_{71}$BM** blend ratios annealed at different temperatures [a]. Here, J_{SC} is the short-circuit current density, V_{OC} is the open-circuit voltage, *FF* is the fill factor, and η is the overall power conversion efficiency.

Blend Ratio	Annealing Temp [°C]	J_{SC} [mA cm^{-2}]	V_{OC} [V]	*FF*	η [%]
60-40	As-cast	1.5	0.96	0.24	0.33
60-40	80	8.9	0.92	0.38	3.1
60-40	100	9.9	0.92	0.42	3.8
60-40	110	10.0	0.92	0.48	4.4
60-40	150	8.3	0.92	0.46	3.5
30-70	As-cast	6.7	0.90	0.38	2.3
30-70	100	5.7	0.90	0.38	2.0
50-50	As-cast	4.8	0.94	0.35	1.6
50-50	100	8.4	0.90	0.45	3.4
60-40	As-cast	1.5	0.96	0.24	0.3
60-40	100	9.9	0.92	0.42	3.8
70-30	As-cast	0.8	0.88	0.26	0.2
70-30	100	9.0	0.94	0.49	4.2

[a] The architecture is ITO/PEDOT:PSS/**DPP(TBFu)$_2$:PC$_{71}$BM**/Al for all devices.

Figure 5c and d shows the *J–V* and the IPCE characteristics of **DPP(TBFu)$_2$:PC$_{71}$BM** devices annealed at 100 °C for 10 min as a function of the blend ratios. The V_{OC} remains the same for all the blend ratios studied here. Before annealing, J_{SC} is highest (6.7 mA cm^{-2}) for large acceptor concentrations (70% by weight). After annealing at 100 °C, J_{SC} increases with the donor concentration from 5.7 mA cm^{-2} for 30:70 blend ratio to 8.4 mA cm^{-2} for 50:50 ratio, and reaches the highest value of 9.9 mA cm^{-2} for the 60:40 blend ratio (Table 1). J_{SC} drops slightly to 9.0 mA cm^{-2} at higher donor concentration (70:30). The *FF* increases with increasing donor concentration from 0.38 for 30:70 to 0.49 for 70:30 (Table 1), which is likely due to a greater balance of charge carrier mobilities at high donor concentrations.[1,11,23] A PCE of 4.4% occurs at blend ratios of 60:40 or 65:35 after annealing between 100 and 110 °C. The IPCEs observed for different blend ratios after annealing at 100 °C for 10 min are plotted in Figure 5d. The IPCE is around 36% for 30:70 blend ratio, increases to ~50% for the 50:50 blend, reaches a maximum value of 58% for the 60:40 blend, and drops to 47% for the 70:30 blend.

The photovoltaic characteristics for different blend ratios and annealing temperatures are summarized in Table 1. Comparing the as-cast devices at different donor:acceptor ratios show a large drop in the device efficiency with increasing donor concentration from 2.3% for the 30:70 blend to 1.6% for the 50:50 blend, to 0.3 for the 60:40 blend, and to 0.18% for the 70:30 blend. Perhaps, this drop in the efficiency is a result of a reduction in electron mobility with lower **PC$_{71}$BM** concentration in the blend (2×10^{-5} cm^2 V^{-1} s^{-1} for 70:30 and 200×10^{-5} cm^2 V^{-1} s^{-1} for 30:70). At low donor concentration (30:70 blend), annealing at 100 °C causes the J_{SC} to drop slightly from 6.7 mA cm^{-2} to 5.7 mA cm^{-2} whereas the *FF* remains unchanged; thus, the efficiency decreases slightly from 2.3% to 2.0%. The drop in J_{SC} may be due to an increase in phase

separation upon thermal annealing, as observed in the AFM image shown in Fig. 4a. Increasing the donor concentration in the blend leads to better J_{SC}, *FF*, and device efficiency (Table 1). The highest performance observed occurred for the 60:40 blend annealed at 110 °C, yielding a J_{SC} of 10 mA cm^{-2}, a V_{OC} of 0.92 V, a *FF* of 0.48, and a PCE of 4.4%. This result is reproducible from three different donor batches with PCE of 4.4 ± 0.4%. This suggests that percolation paths are not optimized at lower temperatures. Future work will focus on understanding the photophysics of the material and developing processing techniques to enhance the formation of percolation paths while maintaining small domain sizes for increased J_{SC} and *FF* values.

3. Conclusions

In summary, we present a novel, small-molecule donor system featuring the DPP−OT chromophoric core whose optical and electronic properties can be tuned by choosing the appropriate terminating group. By using benzofuran units, a solution-processable donor system with high optical density is obtained. Our molecular design gives a material that has a deeper HOMO than the widely used polymeric donor material P3HT but has larger spectral coverage. The frontier orbitals of this donor system are appropriately match with the common fullerene acceptor **$PC_{71}BM$**, which results in effective charge transfer process. **DPP(TBFu)$_2$** films in pure form or when blended with **$PC_{71}BM$** exhibit increased crystallinity upon thermal annealing. With all these properties in consideration, solar cells giving high V_{OC} values and PCE values greater than 4% have been demonstrated, which, to date, are the highest reported BHJ solar cells based on solution-processable conjugated molecular systems. This work demonstrates that the correct combination of conjugated building blocks can lead to small molecules that have excellent film-forming properties for use in BHJ devices. It is expected that with more fine tuning of DPP-based materials, combined with optimized device processing methods, BHJ solar cells with efficiencies of larger than 5% are possible.

4. Experimental

3,6-bis(5-(benzofuran-2-yl)thiophen-2-yl)-2,5-bis(2-ethylhexyl)pyrrolo[3,4-c]pyrrole-1,4-dione (DPP(TBFu)2): In a three-necked, oven-dried 100 mL round-bottom flask, 3,6-bis-(5-bromo-thiophen-2-yl)-2,5-di-n-octyl-pyrrolo[3,4-c]pyrrole-1,4-dione [19] (0.683 g, 1.00 mmol) was mixed with 15 mL of anhydrous toluene and 10 mL of 2.0 M potassium phosphate and the resulting mixture was degassed for 10 min. Benzofuran-2-boronic acid (0.375 g, 2.25 mmol), tris(dibenzylideneacetone)dipalladium(0) (14 mg, 0.0153 mmol), and tri-*tert*-butylphosphonium tetrafluoroborate (18 mg, 0.0620 mmol) were then added to the mixture and then degassed again for 5 minutes. The reaction mixture was stirred and heated to 90°C under argon overnight. The reaction mixture was allowed to cool down to room temperature, after which it was poured into 300 mL of methanol and then stirred for 30 min. The precipitated solid was then collected by vacuum filtration and washed with several portions of distilled water, methanol, isopropanol, and petroleum ether. The crude product was purified by flash chromatography using chloroform as eluent, and the solvent was removed in vacuo to obtain a pure product. 3,6-bis(5-(benzofuran-2-yl)thiophen-2-yl)-2,5-bis(2-ethylhexyl)pyrrolo[3,4-c]pyrrole-1,4-dione is formed as a shiny, dark-green powder (yield: 67.2%) with mp 233°C. ^{1}H NMR (250 MHz, $CDCl_3$, ppm) $\delta = 9.01$ (d, $J = 4.0$ Hz, 2H), 7.48-7.61 (m, 6H), 7.20-7.36 (m, 2H), 7.05 (s, 2H), 4.85 (dd, $J = 4.0$ Hz, 0.5 Hz, 4H) 1.98 (m, 2H), 1.20–1.50 (m, 16H), 0.80-1.00 (m, 12H). MS (LR-EI) *m/z*: [M$^+$] calculated for $C_{46}H_{48}N_2N_2O_4S_2$: 756.31, found 756.03. CHN analysis: calcd: C 72.89, H 6.39, N 3.70. found: C 72.35, H 6.33, N 3.88.

Solar cells were fabricated by spin-casting the BHJ active layer onto a 50-nm layer of PEDOT:PSS (H.C. Stark Baytron P 4083) atop Corning 1737 glass patterned with 140 nm of ITO (Thin Film Devices). An 80-nm-thick aluminum cathode was deposited (area 20 mm^2) by thermal evaporation with no heating of the sample (Angstrom Engineering). Unless otherwise stated, the BHJ layer was spin-cast at 2 500 rpm from a solution of **DPP(TBFu)$_2$** and **$PC_{71}BM$** in chloroform at a total solids concentration of 20 mg mL^{-1}. **$PC_{71}BM$** was purchased from Nano-C and used as received. The active layers were determined to be approximately 95-nm thick using an Ambios XP-100 Stylus profilometer. Solar cells were characterized under simulated 100 mW cm^{-2} AM1.5G irradiation from a 300 W Xe arc lamp with an AM1.5 global filter. Simulator irradiance was characterized using a calibrated spectrometer, and illumination intensity was set using an NREL certified silicon diode with an integrated KG1 optical filter; spectral mismatch factors were calculated to be less than 10%. Many devices were fabricated independently by different individuals (B. W. and A. T.) in two separate laboratories. Three different batches of **DPP(TBFu)$_2$** were tested. Quantum efficiencies were measured with a Xe lamp, monochromator, optical chopper, and lock-in amplifier; photon flux was determined by a calibrated silicon photodiode. Device fabrication and testing were done under inert atmosphere in a nitrogen filled glovebox.

UV−Vis absorption spectroscopy was measured on a Shimadzu 2401 diode array spectrometer. AFM images were collected in air under ambient conditions on multiple sets of films using the Innova scanning probe microscope (Veeco). Silicon probes with spring constants of ~5 N m^{-1} and resonant frequencies of 75 KHz (Budget Sensors) were used for tapping mode AFM measurements.

For UPS measurements, 75-nm-thick Au films were thermally deposited on precleaned Si substrates with a thin native oxide. Blend (or pure) solutions were then spin coated at spin speed of 2 000 rpm and concentration of 0.1%. All films were prepared inside a nitrogen-atmosphere glovebox and were transferred via an airtight sample holder to the UPS analysis chamber. Samples were also kept in a high vacuum chamber overnight to remove solvent residues. The UPS analysis chamber was equipped with a hemispherical electron energy analyzer (Kratos Ultra Spectrometer) and was maintained at 1×10^{-9} Torr. The UPS measurements were carried out using the He I ($h\nu = 21.2$ eV) source. During UPS measurements, a sample bias of −9 V was used in order to separate the sample and the secondary edge for the analyzer. To confirm the reproducibility of the UPS spectra, we repeated these measurements twice on each set of samples. Thin-film XRD spectra were recorded using an X'Pert Phillips Material Research Diffractometer (MRD) at 45 kV and 40 mA with a scanning rate of 0.004 degree per second, and Cu Kα radiation (with wavelength $\lambda = 1.5405$ Å) with a 2θ-ω scan configuration.

Hole- or electron-only diodes were fabricated using the architectures: ITO/PEDOT:PSS/**DPP(TBFu)$_2$**:**$PC_{71}BM$**/Au for holes and Mg/**DPP(TBFu)$_2$**:**$PC_{71}BM$**/Mg for electrons. Electron-mobility measurements were repeated using the architecture of Al/**DPP(TBFu)$_2$**:**$PC_{71}BM$**/Ba/Al. Electron mobilities were measured using electrodes with different work functions to ensure that the built-in potential of the devices did not affect the results. Mobilities were extracted by fitting the current density–voltage curves using the Mott–Gurney relationship (space charge limited current).

Acknowledgements

The authors thank the Office of Naval Research, the Department of Energy, and the Camille Dreyfus Teacher-Scholar Awards Program. B.W. thanks the National Science Foundation Integrative Graduate Education and Research Traineeship program for financial support as well as Jeff Peet for helpful discussions. T.-Q. N. is an Alfred P. Sloan Foundation Research Fellow. M. T. thanks the Royal Thai Government Scholarship for financial support. Correspondence and requests for materials should be addressed to

T.-Q. N. Supporting Information is available online at Wiley InterScience or from the authors.

Received: May 13, 2009
Published online: July 28, 2009

[1] M. C. Scharber, D. Muhlbacher, M. Koppe, P. Denk, C. Waldauf, A. J. Heeger, C. J. Brabec, *Adv. Mater.* **2006**, *18*, 789.
[2] Y. Li, Y. Zou, *Adv. Mater.* **2007**, *20*, 2952.
[3] W. Ma, C. Yang, X. Gong, K. Lee, A. J. Heeger, *Adv. Funct. Mater.* **2005**, *15*, 1617.
[4] M. Reyes-Reyes, K. Kim, D. L. Carroll, *Appl. Phys. Lett.* **2005**, *87*, 083506.
[5] Y. Kim, S. Cook, S. M. Tuladhar, S. A. Choulis, J. Nelson, J. R. Durrant, D. D. C. Bradley, M. Giles, I. McCulloch, C.-S. Ha, M. Ree, *Nat. Mater.* **2006**, *5*, 197.
[6] Q. Wei, T. Nishizawa, K. Tajima, K. Hashimoto, *Adv. Mater.* **2008**, *20*, 2211.
[7] G. Li, V. Shrotriya, J. Huang, Y. Yao, T. Moriarty, K. Emery, Y. Yang, *Nat. Mater.* **2004**, *4*, 864.
[8] M. Campoy-Quilles, T. Ferenczil, T. Agostinelli, P. G. Etchegoin, Y. Kim, T. D. Anthopoulos, P. N. Stavrinou, D. D. C. Bradley, J. Nelson, *Nat. Mater.* **2008**, *7*, 158.
[9] S. Gunes, H. Neugebauer, N. S. Sariciftci, *Chem. Rev.* **2007**, *104*, 1324.
[10] M. T. Lloyd, J. E. Anthony, G. G. Malliaras, *Mater. Today* **2007**, *11*, 34.
[11] B. P. Rand, J. Genoe, P. Heremans, J. Poortmans, *Prog. Photovoltaics: Res. Appl.* **2007**, *15*, 659–676.
[12] J. Roncali, P. Frere, P. Blanchard, R. de Bettignies, M. Turbiez, S. Roquet, P. Leriche, Y. Nicolas, *Thin Solid Films* **2006**, *511–512*, 567.
[13] X. B. Sun, Y. Zhou, W. Wu, Y. Liu, W. Tian, G. Yu, W. Qiu, S. Chen, D. J. Zhu, *J. Phys. Chem. B* **2006**, *110*, 7702.
[14] N. Kopidakis, W. J. Mitchell, J. van de Lagemaat, D. S. Ginley, G. Rumbles, S. E. Shaheen, *Appl. Phys. Lett.* **2008**, *89*, 103524.
[15] M. T. Lloyd, A. C. Mayer, S. Subramanian, D. A. Mourey, D. J. Herman, A. Bapat, V. J. E. Anthony, G. G. Malliaras, *J. Am. Chem. Soc.* **2007**, *129*, 9144.
[16] P. F. Xia, X. J. Feng, J. Lu, S.-W. Tsang, R. Movileanu, Y. Tao, M. S. Wong, *Adv. Mater.* **2008**, *20*, 4810.
[17] S. Roquet, A. Cravino, P. Leriche, O. Alévêque, P. Frère, J. Roncali, *J. Am. Chem. Soc.* **2006**, *128*, 3459.
[18] F. Silvestri, M. D. Irwin, L. Beverina, A. Facchetti, G. A. Pagani, T. J. Marks, *J. Am. Chem. Soc.* **2008**, *130*, 17640.
[19] N. M. Kronenberg, M. Deppisch, F. Wurthner, H. W. A. Lademann, K. Deing, K. Meerholz, *Chem. Commun.* **2008**, 6489.
[20] T. Rousseau, A. Cravino, T. Bura, G. Ulrich, R. Ziessel, J. Roncali, *Chem. Commun.* **2009**, 1673.
[21] M. Fujitsuka, A. Masuhara, H. Kasai, H. Oikawa, H. Nakanishi, O. Ito, T. Yamashiro, Y. Aso, T. Otsubo, *J. Phys. Chem. B.* **2001**, *105*, 9930.
[22] D. M. Delongchamp, S. Sambasivan, D. A. Fischer, E. K. Lin, P. Chang, A. R. Murphy, J. M. J. Fréchet, V. Subramanian, *Adv. Mater.* **2005**, *17*, 2340.
[23] A. J. J. M. van Breeman, P. T. Herwig, C. H. T. Chlon, J. Sweelssen, H. F. M. Schoo, S. Setayesh, W. M. Hardeman, C. A. Martin, D. M. de Leeuw, J. J. P. Valeton, C. W. M. Bastiaansen, D. J. Broer, A. R. Popa-Merticaru, S. C. J. Meskers, *J. Am. Chem. Soc.* **2006**, *128*, 2336.
[24] A. B. Tamayo, M. Tantiwiwat, B. Walker, T.-Q. Nguyen, *J. Phys. Chem. C* **2008**, *112*, 15543.
[25] M. Tantiwiwat, A. B. Tamayo, N. Luu, X.-D. Dang, T.-Q. Nguyen, *J. Phys. Chem. C* **2008**, *112*, 17402.
[26] A. B. Tamayo, B. Walker, T.-Q. Nguyen, *J. Phys. Chem. C* **2008**, *2*, 11545.
[27] A. B. Tamayo, X.-D. Dang, B. Walker, J. H. Seo, T. Kent, T.-Q. Nguyen, *Appl. Phys. Lett.* **2009**, *94*, 063302.
[28] N. Blouin, A. Michaud, D. Gendron, S. Wakim, E. Blair, R. Neagu-Plesu, M. Bellette, G. Durocher, Y. Tao, M. Leclerc, *J. Am. Chem. Soc.* **2008**, *130*, 732.
[29] C. J. Brabec, A. Cravino, D. Meissner, N. S. Sariciftci, T. Fromherz, M. T. Rispens, L. Sanchez, J. C. Hummelen, *Adv. Funct. Mater.* **2001**, *11*, 374.
[30] A. Gadisa, M. Svensson, M. R. Andersson, O. Inganasa, *Appl. Phys. Lett.* **2004**, *84*, 1609.
[31] L. J. A. Koster, V. D. Mihailetchi, P. W. M. Blom, *Appl. Phys. Lett.* **2006**, *88*, 93511.
[32] S. A. Choulis, J. Nelson, Y. Kim, D. Poplavskyy, T. Kreouzis, J. R. Durrant, D. D. C. Bradley, *Appl. Phys. Lett.* **2003**, *83*, 3812.
[33] T. Erb, U. Zhokhavets, G. Gobsch, S. Raleva, B. Stühn, P. Schilinsky, C. Waldauf, C. J. Brabec, *Adv. Funct. Mater.* **2005**, *15*, 1193.
[34] T. Erb, U. Zhokhavetsa, H. Hoppea, G. Gobscha, M. Al-Ibrahimb, O. Ambacherb, *Thin Solid Films* **2006**, *511-512*, 483.
[35] D. Chirvase, J. Parisi, J. C. Hummelen, V. Dyakonov, *Nanotechnology* **2004**, *15*, 1317.
[36] A. Kahn, N. Koch, W. Gao, *J. Polym. Sci. B* **2003**, *41*, 2529.
[37] J. H. Seo, T.-Q. Nguyen, *J. Am. Chem. Soc.* **2008**, *130*, 10042.
[38] K. Akaike, K. Kanai, H. Yoshida, J. Tsutsumi, T. Nishi, N. Sato, Y. Ouchi, K. Seki, *J. Appl. Phys.* **2008**, *104*, 023710.
[39] H. Ishii, K. Sugiyama, E. Ito, K. Seki, *Adv. Mater.* **1999**, *11*, 605.
[40] J. J. Dittmer, R. Lazzaroni, Ph, Leclère, P. Moretti, M. Granström, K. Petritsch, E. A. Marseglia, R. H. Friend, J. L. Brédas, H. Rost, A. B. Holmes, *Sol. Energy Mater. Sol. Cells* **2000**, *61*, 53.
[41] P. Peumans, S. R. Forrest, *Chem. Phys. Lett.* **2004**, *398*, 27.
[42] L. J. A. Koster, V. D. Mihailetchi, P. W. M. Blom, *Appl. Phys. Lett.* **2006**, *88*, 052104.
[43] N. Karl, *Synth. Met.* **2003**, *133–134*, 649.
[44] P. W. M. Blom, M. J. M. de Jong, J. J. M. Vleggaar, *Appl. Phys. Lett.* **1996**, *68*, 3308.
[45] V. D. Mihailetchi, J. K. J. van Duren, P. W. M. Blom, J. C. Hummelen, R. A. J. Janssen, J. M. Kroon, M. T. Rispens, W. J. H. Verhees, M. M. Wienk, *Adv. Funct. Mater.* **2003**, *13*, 43.